

SDSS J133401.39+331534.3: A New Subarcsecond Gravitationally Lensed Quasar¹

Cristian E. Rusu,^{2,3} Masamune Oguri,^{4,5} Naohisa Inada,⁶ Issha Kayo,⁷ Masanori Iye,^{2,3,8} Yutaka Hayano,⁹ Shin Oya,⁹ Masayuki Hattori,⁹ Yoshihiko Saito,⁹ Meguru Ito,⁹ Yosuke Minowa,⁹ Tae-Soo Pyo,⁹ Hiroshi Terada,⁹ Hideki Takami,⁹ and Makoto Watanabe¹⁰

ABSTRACT

The quasar SDSS J133401.39+331534.3 at $z = 2.426$ is found to be a two-image gravitationally lensed quasar with the image separation of $0''.833$. The object is first identified as a lensed quasar candidate in the Sloan Digital Sky Survey Quasar Lens Search, and then confirmed as a lensed system from follow-up observations at the Subaru and University of Hawaii 2.2-meter telescopes. We estimate the redshift of the lensing galaxy to be 0.557 based on absorption lines in the quasar spectra as well as the color of the galaxy. In particular, we observe the system with the Subaru Telescope AO188 adaptive optics with laser guide star,

¹Based on data collected at Subaru Telescope, which is operated by the National Astronomical Observatory of Japan. Use of the UH2.2 m telescope for the observations is supported by NAOJ.

²Optical and Infrared Astronomy Division, National Astronomical Observatory of Japan, 2-21-1, Osawa, Mitaka, Tokyo 181-8588, Japan.

³Department of Astronomy, Graduate School of Science, University of Tokyo 7-3-1, Hongo Bunkyo-ku, Tokyo 113-0033, Japan

⁴Institute for the Physics and Mathematics of the Universe, The University of Tokyo, 5-1-5 Kashiwa-no-ha, Kashiwa, Chiba 277-8568, Japan.

⁵Division of Theoretical Astronomy, National Astronomical Observatory of Japan, 2-21-1, Osawa, Mitaka, Tokyo 181-8588, Japan.

⁶Department of Physics, Nara National College of Technology, Yamatokohriyama, Nara 639-1080, Japan

⁷Department of Physics, Toho University, Funabashi, Chiba 274-8510, Japan.

⁸Department of Astronomical Science, The Graduate University for Advanced Studies (SOKENDAI), National Astronomical Observatory of Japan, 2-21-1, Osawa, Mitaka, Tokyo 181-8588, Japan

⁹Subaru Telescope, National Astronomical Observatory of Japan, 650 North A'ohoku Place, Hilo, Hawaii 96720, USA

¹⁰Department of CosmoSciences, Hokkaido University, Kita 10, Nishi 8, Kita-ku, Sapporo, Hokkaido 060-0810, Japan

in order to derive accurate astrometry, which well demonstrates the usefulness of the laser guide star adaptive optics imaging for studying strong lens systems. Our mass modeling with improved astrometry implies that a nearby bright galaxy $\sim 4''$ apart from the lensing galaxy is likely to affect the lens potential.

Subject headings: gravitational lensing — quasars: individual (SDSS J133401.39+331534.3)
— instrumentation: adaptive optics

1. Introduction

Since the discovery of the first gravitationally lensed quasar (Walsh et al. 1979), it has convincingly been demonstrated that lensed quasars provide insights into various research fields in astrophysics and cosmology, as well as being a unique tool for studying the dark universe. For instance, one can directly measure the structure and substructure of lensing objects, including the distribution of dark matter, through detailed observations and analysis of lensed systems (e.g., Treu & Koopmans 2004; Rusin & Kochanek 2005; Chiba et al. 2005). Magnification by gravitational lensing greatly enhances our ability to study quasar host galaxies at high-redshifts (e.g., Peng et al. 2006). Moreover, the statistics of lensed quasars, as well as measurements of time delays between lensed images, provide independent constraints on cosmological parameters (e.g., Chae et al. 2002; Oguri 2007; Oguri et al. 2008; Suyu et al. 2010).

High resolution imaging such as that provided by Adaptive Optics (AO) is crucial for accurately characterizing lensed quasar systems. This is not only the case for the small-separation systems ($\sim 1''$), where accurate astrometry (prone to the effect of atmospheric seeing) is necessary for constraining mass models of the lensing galaxies (e.g., Sluse et al. 2008), but also for the larger separation systems, where adaptive optics imaging can identify lens substructures and faint extended lensed features such as arcs (e.g., McKean et al. 2007).

The Sloan Digital Sky Survey Quasar Lens Search (SQLS; Oguri et al. 2006, 2008; Inada et al. 2008, 2010) has been one of the most successful strong lens surveys conducted to date. SQLS relies on the large homogeneous sample of spectroscopically-confirmed quasars from the Sloan Digital Sky Survey (SDSS; York et al. 2000). By identifying lensed quasar candidates using the color and morphological information from the SDSS imaging data, SQLS has discovered more than 40 new lensed quasars so far. Together with previously known lenses which were re-observed by the SDSS, the SQLS sample consists of ~ 60 lensed quasars, constituting roughly half of all lensed quasars discovered to date.

However, a disadvantage of SQLS, like other ground-based optical strong lens surveys,

is its poor capability of identifying subarcsecond (image separation $\theta < 1''$) lensed systems. This is because typical seeing sizes of ground-based optical imaging observations are $\sim 1''$, which makes it difficult to resolve multiple components of subarcsecond systems. Indeed, discoveries and confirmations of subarcsecond lensed quasars have been made mostly by radio surveys (e.g., Browne et al. 2003) or by using the Hubble Space Telescope (e.g., Reimers et al. 2002), with few exceptions from ground-based surveys (e.g., Castander et al. 2006; Blackburne et al. 2008).

In this paper, we report the discovery of the first new subarcsecond (two-image) lensed quasar discovered in the course of SQLS, SDSS J133401.39+331534.3 (hereafter SDSS J1334+3315). After briefly describing the lens candidate selection from the SDSS data (§2), we present our imaging and spectroscopic follow-up observations (§3). We further observe this system with the Subaru Telescope laser guide star adaptive optics (LGS+AO188), for robust detection as well as characterization of the lensing galaxy (§4, §5). The accurate astrometry obtained with the LGS+AO188 is then used for gravitational lens mass modeling (§6). We summarize our results in §7. We assume the concordance cosmology with $H_0 = 70 \text{ km}^{-1} \text{ s}^{-1} \text{ Mpc}^{-1}$, $\Omega_m = 0.27$ and $\Omega_\Lambda = 0.73$ throughout this paper.

2. Candidate Selection from the Sloan Digital Sky Survey

The SDSS (SDSS-I and SDSS-II Legacy Survey; York et al. 2000) is a combination of imaging and spectroscopic surveys to map 10,000 square degrees of the sky, centered at the North Galactic Cap. The survey uses a dedicated wide-field 2.5-meter telescope (Gunn et al. 2006) at the Apache Point Observatory in New Mexico, USA. Images taken in five broad-band filters (*ugriz*, Fukugita et al. 1996; Gunn et al. 1998; Doi et al. 2010) are reduced with an automated pipeline, achieving astrometric accuracy better than about $0''.1$ (Pier et al. 2003), and photometric zeropoint accuracy better than about 0.01 magnitude over the entire survey area, in the *g*, *r*, and *i* bands (Hogg et al. 2001; Smith et al. 2002; Ivezić et al. 2004; Tucker et al. 2006; Padmanabhan et al. 2008). The SDSS also conducts spectroscopic observations with a multi-fiber spectrograph covering 3800 Å to 9200 Å, with a resolution of $R \sim 1800$ (Blanton et al. 2003). The data are made publicly available (Stoughton et al. 2002; Abazajian et al. 2003, 2004, 2005, 2009; Adelman-McCarthy et al. 2006, 2007, 2008).

The SQLS (Oguri et al. 2006, 2008; Inada et al. 2008, 2010) identifies lensed quasar candidates among spectroscopic quasars in the SDSS (Richards et al. 2002), using two selection algorithms. One is the morphological selection, which selects quasars with possible extended morphology as small-separation lensed candidates. The other is the color selection, which searches for nearby stellar objects whose colors are similar to the spectroscopically identified

quasars. SDSS J1334+3315 is a lensed quasar candidate at $z = 2.426$ selected by the morphological selection (see Figure 1 for a finding chart). Although the morphological selection is designed to be nearly complete at $\theta > 1''$, it can identify some subarcsecond lensed systems as well, as explicitly shown in simulations of lensed quasar images (Oguri et al. 2006). The point spread function (PSF) magnitudes of the unresolved SDSS J1334+3315 system, measured by the SDSS, are $u = 19.32 \pm 0.03$, $g = 18.76 \pm 0.01$, $r = 18.66 \pm 0.02$, $i = 18.80 \pm 0.02$, and $z = 18.71 \pm 0.03$, where the Galactic extinction is not corrected.

3. Follow-up Spectroscopy and imaging

3.1. Spectroscopy

We conducted spectroscopic follow-up observations of SDSS J1334+3315 with the Faint Object Camera and Spectrograph (FOCAS; Kashikawa et al. 2002) at the Subaru 8.2-meter telescope on January 31, 2009. We adopted the 300B grism and the L600 filter to cover the wavelength from 3700 Å to 6000 Å. We obtained data with an exposure of 600 s using a $1''$ slit, with 2×2 on-chip binning. The resulting spatial resolution is $0''.208 \text{ pixel}^{-1}$, and the spectral resolution is $R \sim 400$. The observations were necessary in order to extract individual spectra of the two stellar components (the two quasar images), which are unresolved in the original SDSS spectroscopy. The one-dimensional spectra of the stellar components were extracted using standard IRAF tasks. We were unable to extract the spectrum of a lensing galaxy (see §3.2), due to its faint nature and the subarcsecond separation of the quasar components. Although the two stellar components are resolved reasonably well in the two-dimensional spectrum, we adopted a deblending procedure developed by Pindor et al. (2006) in extracting one-dimensional spectra, in order to minimize the cross-contamination between the two components.

The spectra shown in Figure 2 indicate that both stellar components have quasar broad emission lines (Ly α , Si IV, C IV) at the same wavelengths, corresponding to a redshift of 2.426 (measured also by the initial SDSS spectroscopy). The emission lines have the same overall shape, supporting the gravitational lensing hypothesis. Several absorption lines are also observed in both spectra, at the same wavelengths. We identify some of these as the 2599 Å Fe II and the 2796 Å, 2803 Å Mg II doublet, from which we derive the redshift of the absorber to be $z = 0.557$. The absorption is seen in both components, with the absorption in component A being slightly stronger than that in component B. We postulate this absorber to be the lensing galaxy, as the redshift is consistent with the photometric redshift estimate of the lensing galaxy, as we will discuss later (§5). In addition, we identify a strong C IV absorber at $z = 2.172$ in both stellar components.

The ratio of the fluxes of the two stellar components is quite constant along the plotted range ($B/A = 0.7 - 0.8$). There is therefore no sign of differential dust reddening which, should it occur on the line of sight to one of the quasars, would affect the flux ratio towards shorter wavelengths. Because the flux ratio is quite constant both across the continuum and the broad line regions, there is also no evidence of microlensing effects. Microlensing due to stars in the lensing galaxy would effect the continuum emission more strongly than the broad line emission, since the physical size of the region associated with the former is much smaller than the one associated with the latter (e.g., Sluse et al. 2008). The change in flux ratio below $\sim 4000 \text{ \AA}$ in the observer’s frame is thought to be due to errors arising from the low detector response in that region.

3.2. Optical and Near-Infrared Imaging

Optical (I and z) follow-up images were taken with the Tektronix 2048×2048 CCD camera (Tek2k) at the University of Hawaii 2.2-meter (UH88) telescope on 2009 April 15. The pixel scale is $0''.219 \text{ pixel}^{-1}$. The total exposure time was 800 s for each filter. The seeing was $\sim 1'' - 1''.2$. The images were reduced using standard IRAF¹ tasks. The photometric zero-points were derived by comparing magnitudes of nearby stars located in the same frame to their SDSS magnitudes, with the resulting zero-point accuracy of $\sim 0.05 \text{ mag}$. For the I band, the magnitude conversion has been performed using the equations of Lupton 2005.²

In addition, we obtained near-infrared (JHK_s) images with the Multi-Object InfraRed Camera and Spectrograph (MOIRCS; Ichikawa et al. 2006; Suzuki et al. 2008) at the Subaru 8.2-meter telescope (Iye et al. 2004) on 2010 April 2, under an excellent seeing size of $\sim 0''.4$. The pixel scale is $0''.117 \text{ pixel}^{-1}$. The total exposure time was 600 s for J and K_s bands, and 480 s for H band. We use the MCSRED software package (I. Tanaka et al., in preparation) for the data reduction. We derived the magnitude zero-points using the standard star FS33 (Leggett et al. 2006), leading to a zero-point accuracy estimated at $\sim 0.05 \text{ mag}$.

Results of the follow-up imaging are summarized in Figure 3. In addition to the candidate lensed quasar system, there are two red galaxies (G1 and G2) within $5''$. In order to check the presence of the lensing galaxy in between the stellar components, as well as to extract relative astrometry and photometry from the data, we analyze the images using

¹IRAF is distributed by the National Optical Astronomy Observatories, which are operated by the Association of Universities for Research in Astronomy, Inc., under cooperative agreement with the National Science Foundation.

²<http://www.sdss.org/dr5/algorithms/sdssUBVRITransform.html>

the public software GALFIT (Peng et al. 2002). We fit all components simultaneously with nearby stars as PSF templates and galaxies modeled by the Sérsic profile. For the bright galaxy G1, the preliminary GALFIT fitting produces the best-fit Sérsic index of $n = 0.87$, very close to the canonical value $n = 1$ for disk-like galaxies. The faint galaxy G2 appears to be quite red, and is also not detected in the optical images. Due to its faintness, we cannot extract an accurate Sérsic index.

Table 1 provides a summary of the GALFIT modeling results. The separation between the stellar components (the two quasar images), derived from the K_s -band image, is $0''.83 \pm 0''.01$. We detect an extended object (galaxy G) in between the two stellar components (the two quasar images), which can be interpreted as a lensing galaxy. We find that the lensing galaxy is hardly detected in the UH88 optical images, while it is significantly detected in the Subaru/MOIRCS near-infrared images (see also Figure 3). The difference can be attributed to the much better angular resolution and the deeper depth of the MOIRCS images. The position of the lensing galaxy G is difficult to determine accurately, as the best fit varies between different bands. However, by adopting the position estimated in the K_s -band, where G appears brightest, we determine that the center of the lensing galaxy is closer to the brighter stellar component, a fact often seen among two-image lensed quasars (e.g., Kayo et al. 2010). We are unable to determine a robust estimate of the Sérsic index for G, due to the galaxy being blended with the quasar components. In order to extract magnitudes for G, we adopt the canonical value for elliptical galaxies, $n = 4$. This is justified by the fact that most galaxies acting as lenses are ellipticals, as spirals only contribute to about 10% of the probability for multiple imaging (e.g., Fukugita & Turner 1991).

4. Laser Guide Star Adaptive Optics Imaging

While the spectroscopic and imaging follow-up observations presented in the previous section indicate that SDSS J1334+3315 is a true lensed quasar system, its small angular separation makes it difficult to study the system in detail solely from these observations. One way to overcome this problem in the near-infrared is to obtain high-resolution adaptive optics images, as already done for several other quasar lens systems (e.g., McKean et al. 2007; Auger et al. 2008; Sluse et al. 2008; Lagattuta et al. 2010).

We obtained high-resolution near-infrared images for this quasar system using the Infrared Camera and Spectrograph (IRCS; Kobayashi et al. 2000) at the Subaru telescope, along with the Laser Guide Star Adaptive Optics system (LGS+AO188; Hayano et al. 2008, 2010; Minowa et al. 2010). AO188 uses a curvature sensor with 188 control elements and a 188 element bimorph deformable mirror (BIM188), and operates at the Nasmyth focus of

the Subaru Telescope. IRCS was used in the low resolution mode with a pixel scale $0''.0527$, producing a $54''$ field of view. The observations were performed in an engineering run on 2011 February 18, with excellent seeing $\sim 0''.3 - 0''.5$. We used an $R \sim 13.4$ mag star located $57''$ from the target as a tip-tilt guide star (see Figure 1). We obtained a set of 60 s individual exposures with a total exposure time of 10 min for J -band, 4 min for H -band, and 12 min in K' -band. The measured Strehl ratios were $\sim 8\%$ in J -band, $\sim 12\%$ in H -band, and $\sim 12\%$ in K' -band. The full width at half maximum (FWHM) of the PSF was $\sim 0''.10 - 0''.15$ in all three bands. Therefore, although the PSF is not quite diffraction limited ($\sim 0.06''$ for Subaru Telescope in the K' -band), it is better than what would be obtained with the Hubble Telescope at diffraction limit, in the equivalent band ($\sim 0.22''$).

The standard star P272-D (Leggett et al. 2006) was observed in the same night and at the same airmass with the target, without adaptive optics. Both the target and standard star frames were reduced with the IRCS IMGRED package (Minowa et al. 2005). The zero-points which we estimate from aperture photometry are $J = 24.39 \pm 0.01$ mag/s, $H = 24.53 \pm 0.02$ mag/s, and $K' = 23.78 \pm 0.02$ mag/s, respectively, where the quoted errors refer only to the differences between aperture photometry of the standard star in different frames.

We initially tried to build the PSF on an isolated star $\sim 10''$ from the target, in the direction opposite to the tip-tilt star. However, this left significant residuals when subtracting the quasar components, most likely due to anisoplanatism introduced by the adaptive optics. We therefore built the PSF by fitting a two-component model, consisting of the Moffat and Gaussian analytical profiles, to the relatively isolated fainter quasar component. Our GALFIT modeling suggests a best-fit Moffat profile FWHM of $\sim 6 - 8$ pixels ($\sim 0''.3 - 0''.4$), which is indicative of the seeing disk, and a Gaussian profile FWHM of $\sim 2 - 3$ pixels ($\sim 0''.10 - 0''.15$), corresponding to the PSF core. This method significantly improves fitting and reduces the residuals after subtracting best-fit models.

We show the adaptive optics images in Figure 4, and summarize the results we obtained in Table 2. Thanks to the much improved angular resolution, the lensing galaxy is clearly visible even before subtracting the stellar components. The spiral arm of the nearby galaxy G1 is also clearly seen. The relative astrometry derived from the LGS+AO188 image is broadly consistent with the MOIRCS result shown in Table 1, but the attached errors are now much smaller. There are small discrepancies in the relative positions of the quasar images, larger than the error bars attached to the MOIRCS measurements, which must be due to an inaccurate original measurement of the position of image A (made difficult by the close proximity of the lens galaxy). The LGS+AO188 measurement corrects the MOIRCS-determined values, because the image A and the lens are more clearly separated. In addition, small (sub-pixel) discrepancies between the MOIRCS- and LGS+AO188-determined positions of galaxies G1

and G2 should be due to better detected morphological features in the LGS+AO188 imaging. The quasar image separation is found to be $\theta = 0''.833 \pm 0.002$. We also confirm that the center of the lensing galaxy is closer to the brighter quasar component. In addition, the high-resolution images enable us to make a more reliable measurement of the shape of each galaxy, such as the half-light radius and the ellipticity. Although the goodness-of-fit estimate χ^2 is almost insensitive to the choice of fiducial Sérsic indices 1 (exponential profile) or 4 (de Vaucouleurs profile), less residuals appear in the K' -band after subtracting the lens galaxy modeled by the Sérsic index 4. This suggests an elliptical galaxy, in accordance with our original assumption.

We must note that the photometry (especially that of the lensing galaxy) differs significantly from the MOIRCS result. This is presumably because of the PSF and magnitude zero-point uncertainties, which are hard to characterize for AO images. On the other hand, relative photometry of the lens - quasar images should be more accurate in the case of the AO observations, due to the higher resolution. Also, objects (especially the galaxies) appear systematically fainter in the AO images, which may be due to uncorrected light scattered at large distances. While we leave for future work more comprehensive and sophisticated analysis of the PSF and photometric calibration, we confirmed that our astrometric results are rather robust against these uncertainties.

5. Photometric redshifts

In order to check the validity of our assumption that the strong absorption at $z = 0.557$ seen in the quasar spectra is caused by the lensing galaxy G, we estimate a photometric redshift for this galaxy based on the magnitudes in the five observed bands ($I, z, J, H, K_s/K'$). We also estimate photometric redshifts for the two nearby galaxy companions. We employ the publicly available HyperZ (Bolzonella et al. 2000) and EAzy (Brammer et al. 2008) algorithms, both of which produce redshift estimates based on template-fitting methods. For both algorithms, we use as templates the observed mean spectral energy distributions (SEDs) of local galaxies from Coleman et al. (1980, hereafter CWW), extrapolated into ultraviolet and near-infrared with the evolutionary models of Bruzual & Charlot (1993). In the case of EAzy, we use a Bayesian prior on the apparent magnitudes, which is implemented in the code. The prior is added to help prevent the redshift probability distributions from having multiple peaks, as template colors can be degenerate with redshift.

Since the best magnitude estimates for the lensing galaxy are significantly different between the MOIRCS JHK_s - and the LGS+AO188 IRCS JHK' -bands, we use both of these estimates separately. On the other hand, for the two nearby galaxies, where the

aperture magnitudes are fairly similar, we use the values obtained with LGS+AO188. As photometric redshift estimates require absolute magnitudes, we attach error bars larger than the ones quoted in Tables 1 and 2, to allow for uncertainties in the magnitude zero-points.

We conducted initial photometric redshift fits with HyperZ, and checked the results of the best-fitted spectral templates with EAzy. The resulting photometric redshift probability distributions computed with EAzy are shown in Figure 5, and summarized in Table 3. For the lensing galaxy, the best-fitted templates obtained with HyperZ are E (elliptical) and Sbc (spiral). The results are consistent with the probability curves calculated by EAzy. Although we cannot conclusively discriminate between the two templates based on the morphological information obtained even with LGS+AO188, both templates yield redshift probability distributions consistent with the redshift estimated from the absorption lines, within 1σ confidence interval when using the LGS+AO188-estimated magnitudes, and at $1-2\sigma$ confidence interval when using MOIRCS-estimated magnitudes. We therefore conclude that the lensing galaxy is likely to be at $z = 0.557$, and is certainly at a redshift lower than that of the quasar components, consistent with the gravitational lensing hypothesis.

For the bright nearby galaxy G1, the probability curve for the Sbc template (matching the disk-like morphology) is in good agreement with $z = 0.557$, making it very likely that this galaxy is located at the same redshift as the lensing galaxy. It is also in good agreement with the previous redshift estimate of 0.50 ± 0.07 , from the SDSS database. The G2 galaxy has a very poorly estimated redshift, due to its faintness, and also appears to be located at a redshift much larger than G and G1.

6. Mass Modeling

We conduct gravitational lensing mass modeling to check whether the observed image configuration can be reproduced with reasonable mass models, as a final check of the gravitational lensing hypothesis for this system. We use the public software *glafic* (Oguri 2010) to solve the lens equation and to find best-fit mass models. We use 7 observational constraints for mass modeling: the (two-dimensional) positions of the lensed quasar images and the lensing galaxy, as well as the flux ratio between the quasar images. The positional constraints are taken from the accurate astrometric results derived from Subaru LGS+AO188 imaging (Table 2). We use a flux ratio constraint of $B/A = 0.75 \pm 0.05$, consistent with most follow-up photometric results as well as the spectroscopic flux ratio over a wide wavelength range. The lens redshift is assumed to be $z = 0.557$. Given the small number of observational constraints available, we are forced to consider the simplest mass models: the Singular Isothermal Ellipsoid (SIE) and the Singular Isothermal Sphere with an external shear (SIS+ γ). Both mass

models have 7 parameters (the position of the lens and its velocity dispersion σ or Einstein radius R_{Ein} , the ellipticity e or shear γ and their associated position angles θ_e or θ_γ , and the position of the source), which indicates that there are no degree of freedom, as is common in the mass modeling of two-image quasar lenses.

We find that both models can fit the lensed system perfectly, signifying that the choice of the models is reasonable. Table 4 summarizes the best-fit values for both models. We find that the best-fit ellipticity for the SIE model, $e = 0.235$, is significantly smaller than the observed ellipticity of the lensing galaxy, $e \sim 0.62$, but the position angles agree quite well with each other. Such large difference of the ellipticity and the agreement of the position angle has often been seen in previous analyses of strong lens systems (e.g., Keeton et al. 1998). The position angle of the best-fit SIS+ γ model is almost the same as that of the SIE model. In fact the angle corresponds to the position of the nearby galaxy G1, suggesting that the quadrupole of the lens potential may be dominated by perturbation due to G1. For both models, the total magnification and time delay are predicted to be $\mu_{tot} \sim 6.0$ and $\Delta t \sim 10 - 11$ days, respectively.

Here we discuss whether galaxy G1 can have a significant impact on the mass modeling. Based on the analysis in Section 5, we assume that the redshift of galaxy G1 is the same as that of the lensing galaxy. The follow-up photometry indicates that G1 is at least ~ 1.5 mag brighter than the lensing galaxy. Adopting the Faber-Jackson relation, we infer that the Einstein radius of G1 is at least twice as large as that of the lensing galaxy, i.e., $R_{Ein} \sim 0''.8$. Given the distance between G and G1 of $d \sim 4''.1$, we estimate the external shear produced by G1 as $\gamma \sim R_{Ein}/2d \sim 0.1$, which is very close to the best-fit external shear of $\gamma \sim 0.096$ for the SIS+ γ model, suggesting that G1 can have a significant impact on this lensed quasar system. A caveat is that G1 appears to be a disk-dominated spiral galaxy (see Figure 4 and Table 2), and hence the use of the Faber-Jackson relation may not be appropriate.

To further explore the origin of the quadrupole, we compute the goodness-of-fit estimate χ^2 as a function of the position angle. Specifically we compute χ^2 for each fixed value of the position angle, with the other model parameters varied to achieve a minimum χ^2 . We find that the results are very similar between the position angle of the ellipticity θ_e , for the SIE model, and the position angle of the external shear θ_γ , for the SIS+ γ model, as a consequence of the well-known shear-ellipticity degeneracy. The result shown in Figure 6 indicates that the position angle inferred from mass modeling is perfectly consistent with an external shear from galaxy G1, as well as consistent with the position angle of the elliptical lensing galaxy G at 1σ level. On the other hand, the location of the nearby galaxy G2 corresponds to an external shear with a large χ^2 , which implies that G2 is not affecting the lens potential. While we cannot decompose contributions from G and G1 at this point,

detailed observations of a lensed host galaxy in deeper adaptive optics imaging observations may help clarify the origin of the quadrupole.

7. Summary

We have reported the discovery of the subarcsecond ($\theta = 0''.833$) gravitationally lensed quasar SDSS J1334+3315. The system has been identified as a lensed candidate from the SDSS data, using the standard SQLS candidate selection algorithm, despite the image separation being smaller than the criterion for which the morphological selection is complete. Our follow-up observations at the Subaru and UH88 telescopes have confirmed the system to be a real strong lensing event. It consists of two images of a quasar at $z = 2.426$, lensed by a foreground galaxy. From the colors as well as absorption lines in the quasar spectra, we infer the redshift of the lensing galaxy to be $z = 0.557$. In particular, we have obtained high-resolution near-infrared images of this lensed quasar system using the Subaru LGS+AO188 system, with a better resolution in the K' -band than would be provided by the Hubble space telescope in the equivalent band. The images clearly reveal the presence of the lensing galaxy in between the quasar images, and enable us to derive very accurate relative astrometry, as well as shapes of galaxies. In particular, the higher resolution made possible to identify errors in the non-adaptive optics astrometry, caused by the lens galaxy and one of the quasar images being blended, and thus made possible a more accurate mass modeling. We have found that the image configuration can well be reproduced with the standard mass models. We have pointed out that the nearby galaxy G1, which is located $< 5''$ from the lensing galaxy and is likely associated physically with the lensing galaxy, may affect the lens potential. This lensed system has the smallest image separation among the newly discovered SQLS lenses.

This work represents the first observation and analysis of any gravitationally lensed quasar system with the Subaru LGS+AO188. Our results demonstrate the usefulness of laser guide star adaptive optics imaging observations, in particular that of the Subaru Telescope LGS+AO188 imaging, which has a much improved sky coverage, for the study of strong lens systems. As explicitly shown, the high-resolution imaging enabled by the adaptive optics system is crucial for accurate and robust measurements of the position and shape of the lensing galaxy, particularly for small-separation lensed quasars as presented in the paper. Indeed we are conducting an imaging survey of SQLS lenses with Subaru LGS+AO188, aiming to derive accurate astrometry and to detect lensed quasar host galaxies, which will further increase the value of the SQLS lensed quasar sample.

CER is sponsored by the Japanese Monbukagakusho scholarship. I.K. acknowledges the support of the JSPS Research Fellowship. This work was supported in part by the FIRST program "Subaru Measurements of Images and Redshifts (SuMIRe)" and World Premier International Research Center Initiative (WPI Initiative), MEXT, Japan. The Subaru LGS+AO188 project has been supported by the Grant-in-Aid for Specially Promoted Research 14002009 from the Japan Ministry of Education, Culture, Sports, Science, and Technology and by the Grant-in-Aid for Scientific research (S)19104004 from Japan Society for the Promotion of Science. The authors recognize and acknowledge the very significant cultural role and reverence that the summit of Mauna Kea has always had within the indigenous Hawaiian community. We are most fortunate to have the opportunity to conduct observations from this superb mountain.

Funding for the SDSS and SDSS-II has been provided by the Alfred P. Sloan Foundation, the Participating Institutions, the National Science Foundation, the U.S. Department of Energy, the National Aeronautics and Space Administration, the Japanese Monbukagakusho, the Max Planck Society, and the Higher Education Funding Council for England. The SDSS Web Site is <http://www.sdss.org/>.

The SDSS is managed by the Astrophysical Research Consortium for the Participating Institutions. The Participating Institutions are the American Museum of Natural History, Astrophysical Institute Potsdam, University of Basel, Cambridge University, Case Western Reserve University, University of Chicago, Drexel University, Fermilab, the Institute for Advanced Study, the Japan Participation Group, Johns Hopkins University, the Joint Institute for Nuclear Astrophysics, the Kavli Institute for Particle Astrophysics and Cosmology, the Korean Scientist Group, the Chinese Academy of Sciences (LAMOST), Los Alamos National Laboratory, the Max-Planck-Institute for Astronomy (MPIA), the Max-Planck-Institute for Astrophysics (MPA), New Mexico State University, Ohio State University, University of Pittsburgh, University of Portsmouth, Princeton University, the United States Naval Observatory, and the University of Washington.

REFERENCES

- Abazajian, K., et al. 2003, AJ, 126, 2081
- Abazajian, K., et al. 2004, AJ, 128, 502
- Abazajian, K., et al. 2005, AJ, 129, 1755
- Abazajian, K. N., et al. 2009, ApJS, 182, 543

- Adelman-McCarthy, J. K., et al. 2006, *ApJS*, 162, 38
- Adelman-McCarthy, J. K., et al. 2007, *ApJS*, 172, 634
- Adelman-McCarthy, J. K., et al. 2008, *ApJS*, 175, 297
- Auger, M. W., Fassnacht, C. D., Wong, K. C., Thompson, D., Matthews, K., & Soifer, B. T. 2008, *ApJ*, 673, 778
- Blackburne, J. A., Wisotzki, L., & Schechter, P. L. 2008, *AJ*, 135, 374
- Blanton, M. R., Lin, H., Lupton, R. H., Maley, F. M., Young, N., Zehavi, I., & Loveday, J. 2003, *AJ*, 125, 2276
- Bolzonella, M., Miralles, J.-M., & Pelló, R. 2000, *A&A*, 363, 476
- Brammer, G. B., van Dokkum, P. G., & Coppi, P. 2008, *ApJ*, 686, 1503
- Browne, I. W. A., et al. 2003, *MNRAS*, 341, 13
- Bruzual A., G., & Charlot, S. 1993, *ApJ*, 405, 538
- Castander, F. J., Treister, E., Maza, J., & Gawiser, E. 2006, *ApJ*, 652, 955
- Chae, K.-H., et al. 2002, *Physical Review Letters*, 89, 151301
- Chiba, M., Minezaki, T., Kashikawa, N., Kataza, H., & Inoue, K. T. 2005, *ApJ*, 627, 53
- Coleman, G. D., Wu, C.-C., & Weedman, D. W. 1980, *ApJS*, 43, 393
- Doi, M., et al. 2010, *AJ*, 139, 1628
- Fukugita, M., & Turner, E. L. 1991, *MNRAS*, 253, 99
- Fukugita, M., Ichikawa, T., Gunn, J. E., Doi, M., Shimasaku, K., & Schneider, D. P. 1996, *AJ*, 111, 1748
- Gunn, J. E., et al. 1998, *AJ*, 116, 3040
- Gunn, J. E., et al. 2006, *AJ*, 131, 2332
- Hayano, Y., et al. 2008, *Proc. SPIE*, 7015, 25
- Hayano, Y., et al. 2010, *Proc. SPIE*, 7736, 21
- Hogg, D. W., Finkbeiner, D. P., Schlegel, D. J., & Gunn, J. E. 2001, *AJ*, 122, 2129

- Ichikawa, T., et al. 2006, *Proc. SPIE*, 6269, 38
- Inada, N., et al. 2008, *AJ*, 135, 496
- Inada, N., et al. 2010, *AJ*, 140, 403
- Ivezić, Ž., et al. 2004, *Astronomische Nachrichten*, 325, 583
- Iye, M., et al. 2004, *PASJ*, 56, 381
- Kashikawa, N., et al. 2002, *PASJ*, 54, 819
- Kayo, I., Inada, N., Oguri, M., Morokuma, T., Hall, P. B., Kochanek, C. S., & Schneider, D. P. 2010, *AJ*, 139, 1614
- Keeton, C. R., Kochanek, C. S., & Falco, E. E. 1998, *ApJ*, 509, 561
- Kobayashi, N., et al. 2000, *Proc. SPIE*, 4008, 1056
- Lagattuta, D. J., Auger, M. W., & Fassnacht, C. D. 2010, *ApJ*, 716, L185
- Leggett, S. K., et al. 2006, *MNRAS*, 373, 781
- McKean, J. P., et al. 2007, *MNRAS*, 378, 109
- Minowa, Y., et al. 2005, *ApJ*, 629, 29
- Minowa, Y., et al. 2010, *Proc. SPIE*, 7736, 122
- Oguri, M. 2007, *ApJ*, 660, 1
- Oguri, M. 2010, *PASJ*, 62, 1017
- Oguri, M., et al. 2006, *AJ*, 132, 999
- Oguri, M., et al. 2008, *AJ*, 135, 512
- Padmanabhan, N., et al. 2008, *ApJ*, 674, 1217
- Peng, C. Y., Ho, L. C., Impey, C. D., & Rix, H.-W. 2002, *AJ*, 124, 266
- Peng, C. Y., Impey, C. D., Ho, L. C., Barton, E. J., & Rix, H.-W. 2006, *ApJ*, 640, 114
- Pier, J. R., Munn, J. A., Hindsley, R. B., Hennessy, G. S., Kent, S. M., Lupton, R. H., & Ivezić, Ž. 2003, *AJ*, 125, 1559
- Pindor, B., et al. 2006, *AJ*, 131, 41

- Richards, G. T., et al. 2002, *AJ*, 123, 2945
- Reimers, D., Hagen, H.-J., Baade, R., Lopez, S., & Tytler, D. 2002, *A&A*, 382, L26
- Rusin, D., & Kochanek, C. S. 2005, *ApJ*, 623, 666
- Sluse, D., Courbin, F., Eigenbrod, A., & Meylan, G. 2008, *A&A*, 492, L39
- Smith, J. A., et al. 2002, *AJ*, 123, 2121
- Stoughton, C., et al. 2002, *AJ*, 123, 485
- Suyu, S. H., Marshall, P. J., Auger, M. W., Hilbert, S., Blandford, R. D., Koopmans, L. V. E., Fassnacht, C. D., & Treu, T. 2010, *ApJ*, 711, 201
- Suzuki, R., et al. 2008, *PASJ*, 60, 1347
- Treu, T., & Koopmans, L. V. E. 2004, *ApJ*, 611, 739
- Tucker, D. L., et al. 2006, *Astronomische Nachrichten*, 327, 821
- Walsh, D., Carswell, R. F., & Weymann, R. J. 1979, *Nature*, 279, 381
- York, D. G., et al. 2000, *AJ*, 120, 1579

Table 1. Result of imaging observations with UH88/Tek2k and Subaru/MOIRCS

Name	ΔX [arcsec]	ΔY [arcsec]	I	z	J	H	K_s
A	0.000 ± 0.003	0.000 ± 0.003	19.16 ± 0.03	19.18 ± 0.03	18.57 ± 0.02	18.10 ± 0.02	17.41 ± 0.01
B	-0.502 ± 0.003	0.673 ± 0.003	19.50 ± 0.02	19.75 ± 0.03	18.99 ± 0.02	18.40 ± 0.01	17.72 ± 0.01
G	-0.159 ± 0.015	0.235 ± 0.020	21.50 ± 0.37	21.92 ± 1.69	20.29 ± 0.11	19.30 ± 0.07	18.53 ± 0.06
G1	-3.160 ± 0.004	-2.587 ± 0.004	19.95 ± 0.04	20.33 ± 0.07	18.68 ± 0.03	17.70 ± 0.02	17.06 ± 0.02
G2	1.160 ± 0.011	2.073 ± 0.013	22.18 ± 0.18	20.42 ± 0.08	19.69 ± 0.07

Note. — The positive directions of ΔX and ΔY are defined by West and North, respectively. The astrometry is measured in the K_s -band image. The quoted errors include statistical errors only. The magnitude measurements for galaxies G1 and G2 are photometric aperture magnitudes, whereas those of components A, B, and G are model estimates fitted with GALFIT. The quoted errors include statistical errors only, and exclude uncertainties inherent in the PSF estimates or the zero-points. Magnitudes are given in the Vega system, without the Galactic extinction correction, except for z -band magnitudes which are in the AB system

Table 2. Result of Subaru LGS+AO188 imaging

Name	ΔX [arcsec]	ΔY [arcsec]	n	R_e [arcsec]	e	θ_e [deg]	J	H	K'
A	0.000 ± 0.001	0.000 ± 0.001	\dots	\dots	\dots	\dots	18.71 ± 0.01	18.27 ± 0.01	17.53 ± 0.01
B	-0.484 ± 0.001	0.677 ± 0.001	\dots	\dots	\dots	\dots	19.03 ± 0.01	18.54 ± 0.02	17.83 ± 0.01
G	-0.134 ± 0.006	0.235 ± 0.007	$\equiv 4$	0.20 ± 0.03	0.62 ± 0.08	-42.7 ± 5.9	21.01 ± 0.06^a	20.06 ± 0.05^a	19.36 ± 0.05
G1	-3.178 ± 0.004	-2.578 ± 0.002	1.68 ± 0.06	0.50 ± 0.01	0.53 ± 0.01	-58.2 ± 0.7	18.68 ± 0.04	17.90 ± 0.03	17.28 ± 0.03
G2	1.159 ± 0.005	2.033 ± 0.004	2.46 ± 1.09	0.08 ± 0.01	0.61 ± 0.11	38.3 ± 7.0	22.69 ± 0.31	20.52 ± 0.13	19.94 ± 0.10

Note. — The positive directions of ΔX and ΔY are defined by West and North, respectively, and the astrometry is estimated from the K' -band image. Shapes of the galaxies (the Sérsic index n , the half-light radius R_e , the ellipticity e , and the position angle θ_e measured East of North) are all measured in the K' -band image. The Sérsic index of galaxy G is considered to be the fiducial value of 4, as explained in the text. The magnitude measurements for galaxies G1 and G2 are photometric aperture magnitudes, whereas those of components A, B, and G are model estimates fitted with GALFIT. The quoted errors include statistical errors only, and exclude uncertainties inherent in the PSF estimates or the zero-points. Magnitudes are given in the Vega system, without the Galactic extinction correction.

^aThe quoted values of the lens galaxy magnitudes in the J - and H - bands correspond to the best-fit models (Sérsic index 1 rather than 4). When constraining an index of 4, the values become ~ 0.1 mag lower.)

Table 3. Best-fit photometric redshifts

Object & template	Best-fit z	1σ limits	2σ limits
G (AO), Sbc template	0.694	$0.494 - 0.876$	$0.329 - 1.174$
G (AO), E template	0.586	$0.397 - 0.768$	$0.255 - 0.959$
G (w/o AO), E template	0.694	$0.530 - 0.850$	$0.368 - 1.004$
G (w/o AO), Sbc template	0.818	$0.644 - 0.986$	$0.456 - 1.202$
G1, Sbc template	0.513	$0.390 - 0.642$	$0.298 - 0.757$
G2, all CWW templates	2.124	$1.774 - 2.579$	$1.311 - 2.884$

Table 4. Best-fit mass models

Model	σ [km s $^{-1}$]	e or γ	θ_e or θ_γ [deg]	R_{Ein} [arcsec]	μ_{tot}	Δt [day]
SIE	147	0.235	-47.1	0.40	6.0	11.1
SIS+ γ	143	0.096	-47.2	0.38	6.1	10.0

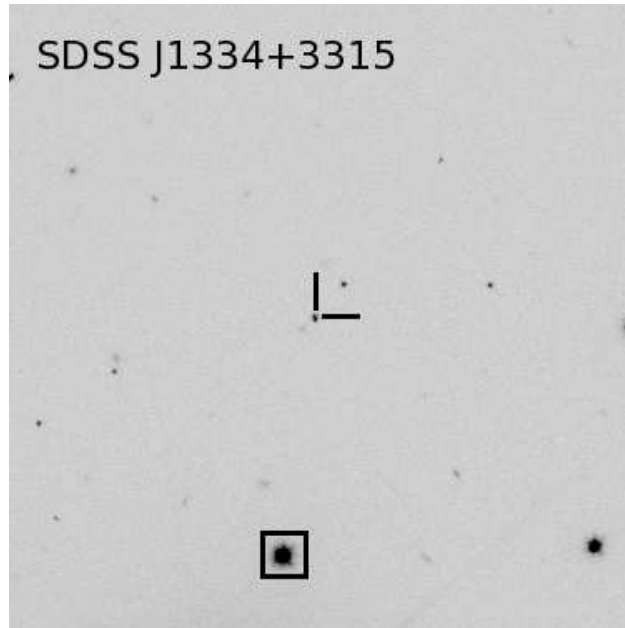


Fig. 1.— Finding chart of SDSS J1334+3315 from the SDSS *i*-band image. The size is $2'.5 \times 2'.5$. North is up and East is left. The bright star indicated by an open square was used as the tip-tilt star for the laser guide star adaptive optics imaging (see §4 for details).

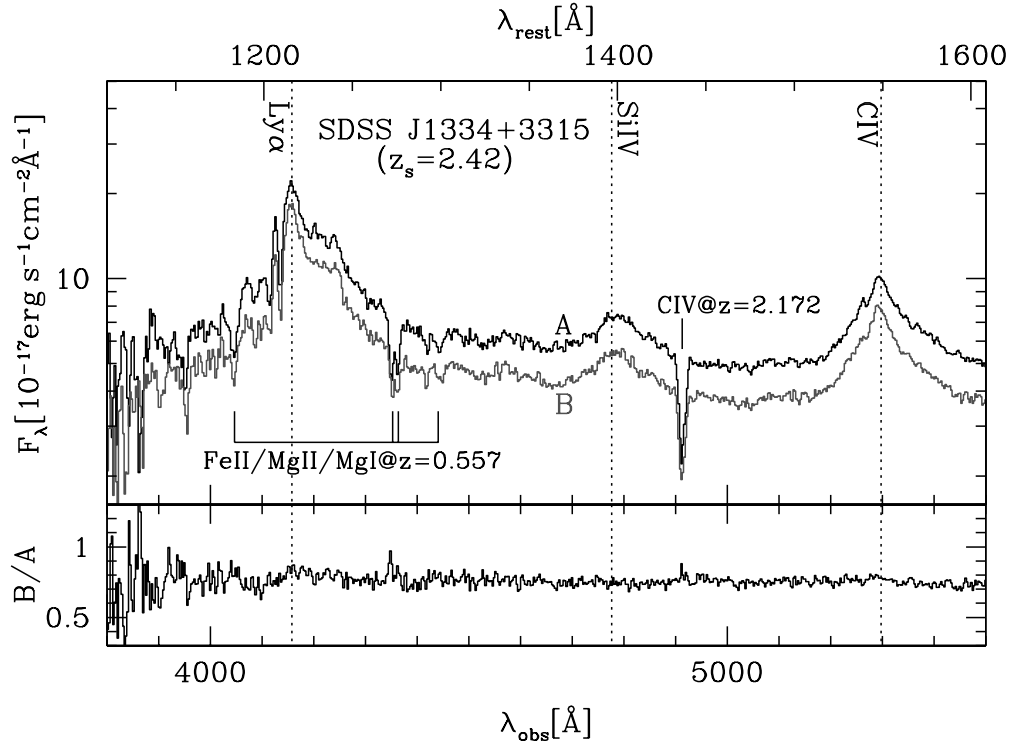


Fig. 2.— Follow-up spectra of SDSS J1334+3315 A and B taken with FOCAS at the Subaru Telescope. Quasar emission lines redshifted to $z_s = 2.42$ are indicated by vertical dotted lines. Strong absorption systems at $z = 0.557$ and 2.172 seen in both component A and B are marked by vertical solid bars. The lower panel plots the ratio of the two spectra.

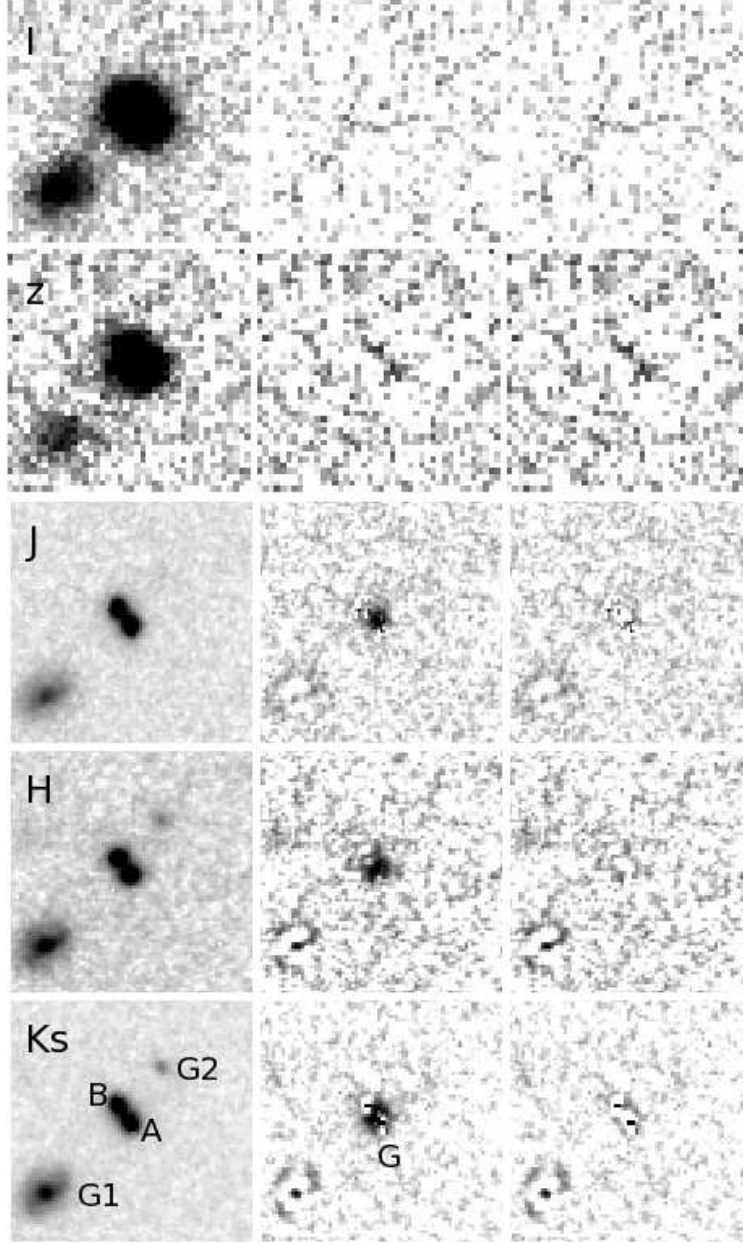


Fig. 3.— Follow-up images taken with Tek2k at the UH88 Telescope and MOIRCS at the Subaru Telescope. The size of each panel is $9'' \times 9''$. North is up and East is left. From top to bottom panels, we show I - and z -band images from Tek2k and J -, H -, and K_s -band images from MOIRCS. Left, middle, and right panels display original images, images after subtracting all but the lensing galaxy (component G), and images after subtracting all components, respectively.

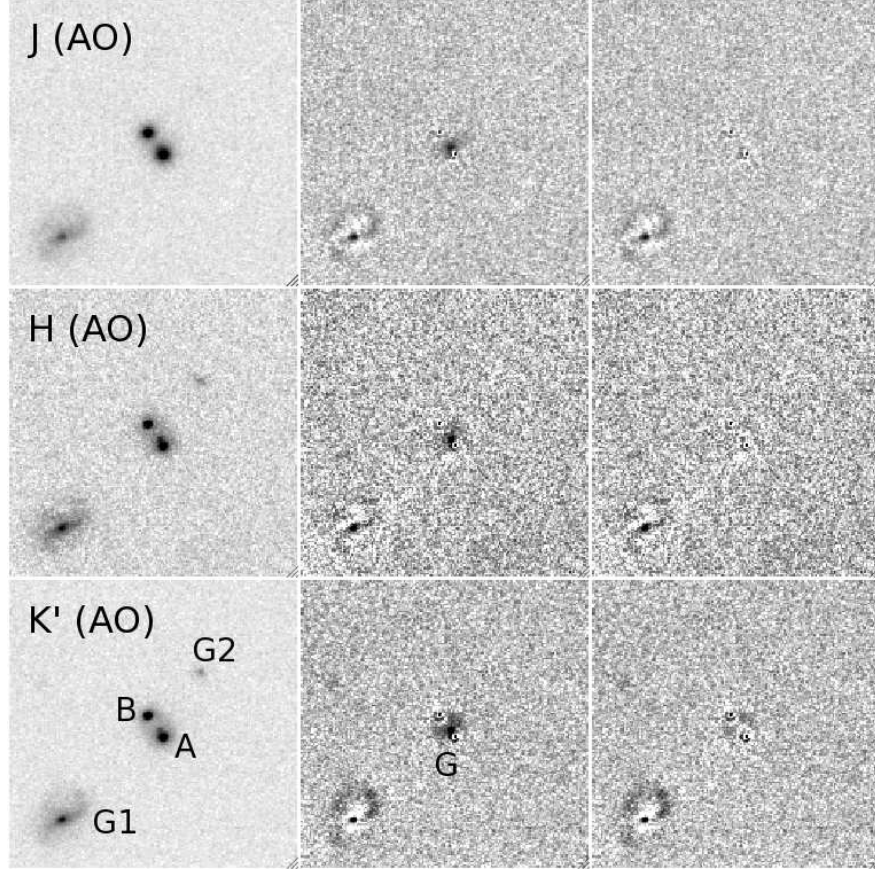


Fig. 4.— Subaru LGS+AO188 images of SDSS J1334+3315 in J -, H -, and K' -bands. The size of each panel is $9'' \times 9''$. North is up and East is left. As in Figure 3, from left to right panels we show original images, images after subtracting all but the lensing galaxy (component G), and images after subtracting all components, respectively.

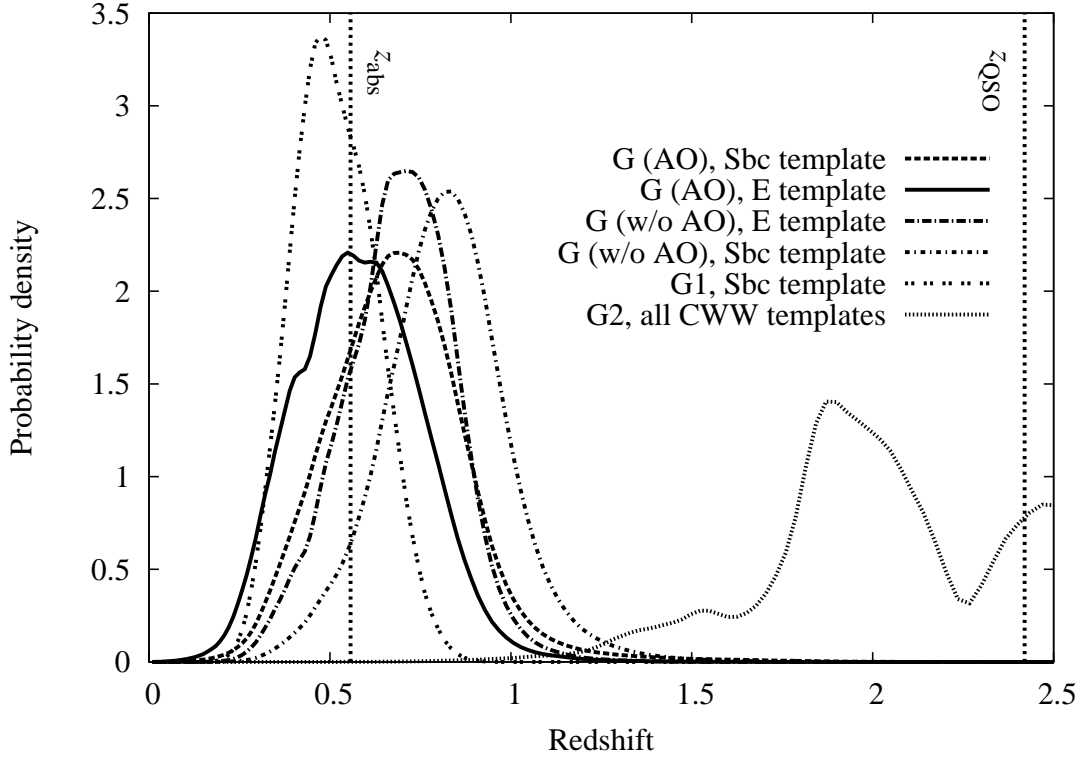


Fig. 5.— Photometric redshift probability distributions, normalized to unit area, for the three galaxies G, G1 and G2, calculated using the magnitudes in Tables 1 and 2. In the case of G, we consider separately the IRCS JHK' (with Adaptive Optics) and MOIRCS JHK_s (w/o AO) magnitudes. The probability distributions are calculated with EAzy, for the most consistent template estimates (see §5 for details). The redshift of the quasar components, as well as that of the absorption line system measured in both quasars at $z = 0.557$, are also marked with vertical lines.

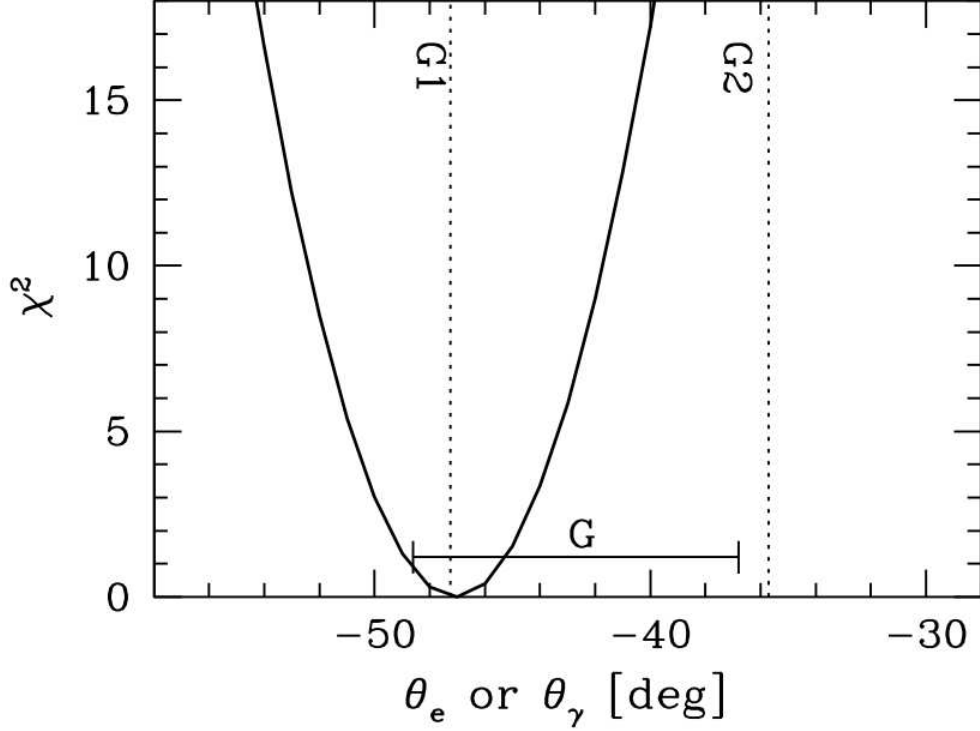


Fig. 6.— The best-fit χ^2 as a function of the position angle measured East of North. Since the results are very similar for SIE and SIS+ γ models, the position angle can be interpreted as either θ_e of SIE or θ_γ of SIS+ γ . Note that the other model parameters are marginalized over. The horizontal line indicates the 1σ range of the measured position angle of the lensing galaxy G. The vertical dotted lines show directions of the external shear corresponding to the location of nearby galaxies G1 and G2.